

Article

# Enhanced Photo-Electrochemical Responses through Photo-Responsive Ruthenium Complexes on ITO Nanoparticle Surface

Uji Pratomo<sup>1,2,\*</sup> , Salmahaminati<sup>3,4</sup>, Minori Abe<sup>3,5</sup>, Masahiko Hada<sup>3</sup> , Santhy Wyantuti<sup>1</sup>, Husein H. Bahti<sup>1</sup> and Jacob Yan Mulyana<sup>2,6,\*</sup>

- <sup>1</sup> Department of Chemistry, Faculty of Mathematics and Natural Sciences, Universitas Padjadjaran, Jl. Raya Bandung Sumedang Km.21, Kabupaten Sumedang 45363, Indonesia; santhy.wyantuti@unpad.ac.id (S.W.); husein.bahti@unpad.ac.id (H.H.B.)
- <sup>2</sup> Department of Applied Chemistry, Graduate School of Urban Environmental Sciences, Tokyo Metropolitan University, 1-1 Minami Osawa, Hachioji 192-0397, Tokyo, Japan
- <sup>3</sup> Department of Chemistry, Graduate School of Science, Tokyo Metropolitan University, 1-1 Minami Osawa, Hachioji 192-0364, Tokyo, Japan; salmahaminati@uui.ac.id (S.); minoria@hiroshima-u.ac.jp (M.A.); hada@tmu.ac.jp (M.H.)
- <sup>4</sup> Department of Chemistry, Faculty of Mathematics and Natural Sciences, Islamic University of Indonesia, Yogyakarta 55581, Indonesia
- <sup>5</sup> Department of Chemistry, Hiroshima University, 1-3-1 Kagamiyama, Higashi Hiroshima City 739-8526, Hiroshima, Japan
- <sup>6</sup> School of Education, Faculty of Arts and Education, Deakin University, 221 Burwood Hwy, Burwood, VIC 3125, Australia
- \* Correspondence: u.pratomo@unpad.ac.id (U.P.); jacob.mulyana@deakin.edu.au (J.Y.M.)

**Abstract:** The mononuclear ruthenium 1-Cl and dinuclear ruthenium 2-Cl complexes undergo a photo-induced ligand exchange in water, affording the corresponding 1-H<sub>2</sub>O and 2-H<sub>2</sub>O complexes. The use of indium tin oxide nanoparticles (*nano*ITOs) to explore the photo-electrochemistry of the in situ-generated 1-H<sub>2</sub>O and 2-H<sub>2</sub>O in solution revealed greater photocurrents produced by these two complexes when compared with an experiment using a buffer only. Interestingly, the high photocurrent shown by the dinuclear complex 2-H<sub>2</sub>O was accompanied by the deposition of its higher oxidation state (H<sub>2</sub>O)Ru<sup>II</sup>-Ru<sup>III</sup>(OH), as evidenced with cyclic voltammetry, SEM and XPS. The IPCE and spectro-electrochemistry studies supported by TD-DFT calculations revealed the visible light harvesting ability of 1-H<sub>2</sub>O and 2-H<sub>2</sub>O in solution and the subsequent electron injection into the conduction band of the *nano*ITOs, enhanced in 2-H<sub>2</sub>O via a plausible chelating effect.

**Keywords:** electrochemistry; photo-electrochemistry; ruthenium complexes; photo-electrochemical devices



**Citation:** Pratomo, U.; Salmahaminati, Abe, M.; Hada, M.; Wyantuti, S.; Bahti, H.H.; Mulyana, J.Y. Enhanced Photo-Electrochemical Responses through Photo-Responsive Ruthenium Complexes on ITO Nanoparticle Surface. *Processes* **2023**, *11*, 2060. <https://doi.org/10.3390/pr11072060>

Academic Editors: Yanan Zhou, Guoshuai Liu and Xiaoping Gao

Received: 23 May 2023

Revised: 3 July 2023

Accepted: 6 July 2023

Published: 10 July 2023



**Copyright:** © 2023 by the authors. Licensee MDPI, Basel, Switzerland. This article is an open access article distributed under the terms and conditions of the Creative Commons Attribution (CC BY) license (<https://creativecommons.org/licenses/by/4.0/>).

## 1. Introduction

The photo-electrochemical (PEC) conversion of water to hydrogen fuel has attracted much interest because of its potential to realize sustainable energy devices that can eventually replace fossil fuels [1–3]. However, electrocatalytic water splitting driven by photon energy has yet to achieve efficiency and durability levels suitable for practical application [4–10]. Perhaps the challenging aspect in this regard is that the water oxidation half reaction ( $2\text{H}_2\text{O} \rightarrow \text{O}_2 + 4\text{H}^+ + 4\text{e}^-$ ) is a difficult process that requires efficient water oxidation catalysts. Despite its energy-demanding nature, the 1.23 V thermodynamic requirement for water oxidation can be driven by light using semiconductors with appropriate band gaps [4], although the main challenge is that most metal oxide semiconductors do not catalyze the water oxidation reaction efficiently. Considerable efforts to improve the efficiency of low-cost semiconductors, such as TiO<sub>2</sub>, BiVO<sub>4</sub> and

$\text{Fe}_2\text{O}_3$ , have recently been undertaken through many different techniques, including heterojunction, band alignment [11–18] and the incorporation of cocatalysts [19–26].

The integration of molecular materials with catalytic and photosensitizing functions is particularly attractive, owing to the easy modification of these materials via synthesis to achieve desired properties, such as a light-harvesting capability up to the near-infrared region [27], properties that are difficult to achieve with semiconductor-only systems. The facile absorption of molecular materials onto the surface of metal oxide semiconductors also allows for the detailed identification of the photophysical properties and energetic factors associated with the charge transfer processes [28–31], which drive the oxidation of chemical species on the photoanode surface [27,32,33]. Our group recently identified that the performance of  $\text{TiO}_2$ -based dye-sensitized photo-electrochemical (DSPEC) devices relies on many factors, such as the ground- and excited-state energies of the photosensitizers, hole mobility, reorganization energy and hydrophobicity [34]. We observed the crucial role of the hole-hopping energetics of the photosensitizer molecules on a  $\text{TiO}_2$  surface that was proven experimentally [34] and through the use of a theoretical calculation [35], which also proved to suppress electron–hole recombination in a  $\text{TiO}_2$ -coated  $\text{BiVO}_4$  system [36].

Despite the advantage of the surface binding of photosensitizer or catalyst molecules through anchoring groups such as phosphonic and carboxylic acids for facilitating an effective charge transfer [37,38], this is often hindered by the fact that the molecules can easily detach from the metal oxide surface in aqueous environments under prolonged light irradiation [38], although we recently found that this can be minimized through a “hydrophobicity” approach, where the ruthenium photosensitizer molecule was structurally modified with a long alkyl chain [34,39].

Although a study of the photo-driven hole and electron transfer using surface-bound ruthenium complexes on indium tin oxide nanoparticles (*nano*ITOs) has been published [40–43], the use of *nano*ITOs for photo-driven water splitting research has not been widely explored, despite having a band gap range (3.5–4.3 eV) suitable for water splitting [44]. In this work, we explore for the first time the photo-electrochemistry of ruthenium complexes using a *nano*ITO working electrode in the metal-oxide–solution interface, as shown in Figure 1a. The novel PEC technique is composed of a mononuclear ruthenium complex  $[\text{Ru}(\text{terpy})(\text{Me}_2\text{bipy})(\text{H}_2\text{O})]^{2+}$  (1- $\text{H}_2\text{O}$ ) and dinuclear  $[\{\text{Ru}(\text{terpy})(\text{H}_2\text{O})\}_2(\mu\text{-bb}_5)]^{4+}$  (2- $\text{H}_2\text{O}$ ) (where  $\text{terpy}$  = 2,2':6',2''-terpyridine;  $\text{Me}_2\text{bipy}$  = 4,4'-dimethyl-2,2'-bipyridine; and  $\text{bb}_5$  = bis[4(4'-methyl-2,2'-bipyridyl)]-1,5-alkane) dissolved in a pH 7 buffer solution, which interacts with light on the electroactive *nano*ITO surface. We present the study of the photo-induced ligand exchange of the precursor complexes  $[\text{Ru}(\text{terpy})(\text{Me}_2\text{bipy})(\text{Cl})]^+$  (1-Cl) and  $[\{\text{Ru}(\text{terpy})(\text{Cl})\}_2(\mu\text{-bb}_5)]^{2+}$  (2-Cl) to the corresponding 1- $\text{H}_2\text{O}$  and 2- $\text{H}_2\text{O}$  complexes, the TD-DFT calculations, electrochemistry and photo-electrochemistry, incident photon to current efficiency (IPCE) and spectro-electrochemistry to reveal the photo-electrochemical properties of the in situ-generated 1- $\text{H}_2\text{O}$  and 2- $\text{H}_2\text{O}$  in the solution-based PEC platform.

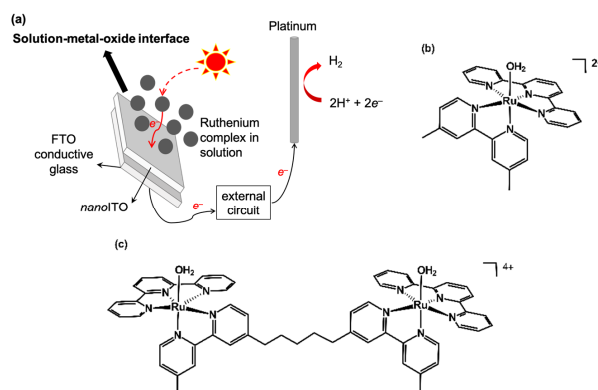


**Figure 1.** (a) Solution-based PEC diagram in the present study; (b) chemical structure of 1- $\text{H}_2\text{O}$ ; (c) chemical structure of 2- $\text{H}_2\text{O}$ .

## 2. Materials and Methods

### 2.1. General

UV/vis spectra were recorded on a Shimadzu UV-2600 spectrometer (Shimadzu, Kyoto, Japan). Fluorescence spectra were recorded on a Jasco FP-6500 spectrofluorometer (Jasco, Tokyo, Japan).  $^1\text{H-NMR}$  spectra were collected at 298 K using a Bruker instrument (500 MHz) (Bruker, Billerica, MA, USA). Electrospray ionization mass spectrometry (ESI-MS) spectra were measured on a Bruker microTOF II mass spectrometer. An elemental analysis was carried out on an Exeter Analytical, Inc. (Chelmsford, MA, USA), CE-440F elemental analyzer. A scanning electron microscopy (SEM) analysis of the electrodes was performed on a JEOL JSM-6100 microscope (JEOL, Tokyo, Japan). XPS data were recorded using a JPS-9010MX photoelectron spectrometer.

### 2.2. Materials

ITO nanoparticles (<100 nm) were purchased from DLS.  $\text{RuCl}_3$  hydrate, 4,4'-Di-tert-butyl-2,2'-bipyridyl and 2,2':6',2''-terpyridine were purchased from Sigma Aldrich (St. Louis, MO, USA). Other chemicals were purchased from Tokyo Chemical Company, Kanto Chemical and Wako (Tokyo, Japan). Organic solvents were dried and distilled according to the standard methods when necessary. The ligand bis[4(4'-methyl-2,2'-bipyridyl)]-1,5-alkane ( $\text{bb}_5$ ) was synthesized according to the reported procedure [45].

### 2.3. Synthesis

The synthesis of the mononuclear  $[\text{Ru}(\text{terpy})(\text{Me}_2\text{bipy})\text{Cl}]\text{Cl}$  (1-Cl) and dinuclear  $[\{\text{Ru}(\text{terpy})(\text{Cl})\}_2(\mu\text{-bb}_5)]\text{Cl}_2$  (2-Cl) complexes was performed according to the previously reported methods with slight modifications [46,47]. The typical procedure was as follows: Solid  $[\text{Ru}(\text{terpy})\text{Cl}_3]$  (0.20 g, 0.45 mmol) and appropriate ligands (0.45 mmol for  $\text{Me}_2\text{bpy}$  and 0.23 mmol for  $\text{bb}_5$ ) were refluxed in  $\text{EtOH}/\text{H}_2\text{O}$  (4:1; 40 mL) for 4 h. After cooling, the solvent mixture was evaporated to dryness. The crude product was dissolved in acetone and loaded onto a silica gel column. The pure complexes were separated from their impurities using  $\text{MeOH}/(\text{CH}_3)_2\text{CO}$  (2:1) as the eluent. The separation of the geometric isomers of  $[\{\text{Ru}(\text{terpy})(\text{Cl})\}_2(\mu\text{-bb}_5)]\text{Cl}_2$  was not attempted.

$[\text{Ru}(\text{terpy})(\text{Me}_2\text{bipy})\text{Cl}]\text{Cl}$ :  $^1\text{H-NMR}$  (500 MHz,  $\text{D}_2\text{O}$ )  $\delta$  9.56 (d,  $J = 5.75$  Hz); 8.38 (d,  $J = 8.15$  Hz); 8.32 (s); 8.25 (d,  $J = 8.1$  Hz); 7.98 (t); 7.74 (t); 7.65 (d,  $J = 5.05$  Hz); 7.58 (d,  $J = 5.1$ ); 7.12 (t); 6.95 (d,  $J = 5.9$  Hz); 2.33 (s); 1.93 (s). ESI-MS: 554.1  $[\text{M}]^+$ . Elemental analysis: Calcd. for  $\text{C}_{27}\text{H}_{23}\text{Cl}_2\text{N}_5\text{Ru}\cdot 4\text{H}_2\text{O}$ : C, 49.02; H, 4.72; N, 10.59. Found: C, 48.41; H, 4.45; N, 10.39.

$[\{\text{Ru}(\text{terpy})(\text{Cl})\}_2(\mu\text{-bb}_5)]\text{Cl}_2$ :  $^1\text{H-NMR}$  (500 MHz,  $\text{D}_2\text{O}$ )  $\delta$  9.59 (s); 9.54 (s); 9.47 (d,  $J = 5.65$  Hz); 9.46 (t); 8.40 (d,  $J = 2.85$  Hz); 8.36 (d,  $J = 11.05$  Hz); 8.25 (m); 8.06 (m); 7.99 (m); 7.66 (m); 7.56 (m); 7.47 (m); 7.37 (t); 7.29 (m); 6.85 (m); 2.59 (m); 2.27 (s); 2.07-2.02 (m); 1.2 (m). ESI-MS: 574.1  $[\text{M}]^+ / 2$ . Elemental analysis: Calcd. for  $\text{C}_{57}\text{H}_{50}\text{Cl}_4\text{N}_{10}\text{Ru}_2\cdot 6\text{H}_2\text{O}$ : C, 51.59; H, 4.71; N, 10.55. Found: C, 51.37; H, 4.67; N, 10.15.

### 2.4. Film Preparation

An ITO paste was produced by blending 15 g of an ITO dispersion (<100 nm (DLS), 30 wt% in isopropanol) with 25 mL 10 wt% ethyl cellulose in ethanol and 20 mL terpineol. The ethanol was evaporated using a rotary evaporator once a completely uniform solution was obtained. The FTO/ITO film (0.81  $\text{cm}^2$  film area and 7 mm thickness) was then created through screen-printing on top of conductive FTO glass and sintering at 450  $^\circ\text{C}$ . The ITO films were then prepared through screen-printing on top of conductive FTO glass, followed by sintering at 450  $^\circ\text{C}$  to obtain an FTO/ITO film (0.81  $\text{cm}^2$  film area and 7  $\mu\text{m}$  thickness).

### 2.5. Electrochemistry and Photo-Electrochemistry

Custom-built glass cells were utilized for conducting the electrochemical and photo-electrochemical experiments. A coiled Pt electrode was used as the counter electrode, while  $\text{Ag}/\text{AgCl}$  (3M NaCl) served as the reference electrode ( $E_{\text{NHE}} = E_{\text{Ag}/\text{AgCl}} + 0.198$ ).

A three-electrode system was connected to a Hokuto Denko Hz-3000 potentiostat, which was controlled through a computer using Hz-3000 software. The complexes were dissolved in a pH 7 phosphate buffer for the electrochemistry experiments, and cyclic and linear sweep voltammetry measurements were taken at a scan rate of  $100 \text{ mV s}^{-1}$ . During the PEC measurements, the *nanoITO* photoanode was illuminated from the front side using a 500 W Xenon light source (Ushio Optical module solar simulator SX-UI500NQ, Ushio, Tokyo, Japan) with a typical light intensity of  $160 \text{ mW cm}^{-2}$ , as measured with a TENMARS TM-208 solar light meter.

### 2.6. Spectro-Electrochemistry

The spectro-electrochemistry was performed manually using on a custom-made glass cell containing FTO/*nanoITO*s at a 1 cm path length. The cell was inserted into a UV-Vis machine and the electrodes were connected to a potentiostat and a computer for potential-controlled measurements. The absorption spectra of the *nanoITO*s in buffer only and that of the aqua complexes were taken at the potentials 0.2 V, 0.6 V, 0.8 V, 1.0 V, 1.2 V, 1.4 V, 1.6 V and 1.7 V. The scans were conducted when the currents were constant.

### 2.7. Gas Measurements

The developed hydrogen gas from the cathodic area was introduced into a Shimadzu GC-8A gas chromatograph, which was equipped with a micropacked RT-MSieve 5A packed column and a TCD detector by utilizing a Vici pressure lock gas syringe. The GC assessments were carried out at a temperature of  $40 \text{ }^\circ\text{C}$  in an oven, utilizing nitrogen gas as a carrier, with an injection temperature of  $120 \text{ }^\circ\text{C}$ . The determination of molecular oxygen was carried out with a Delta Ohm (HD-2109.2) dissolved oxygen meter.

### 2.8. IPCE Measurements

The incident photon-to-charge carrier efficiencies (IPCEs) of the *nanoITO*s in buffer only and in the presence of the aqua complexes were measured in a custom-made three-electrode cell. The cell consisted of a Ag/AgCl reference electrode, FTO/*nanoITO*s as the working electrode and Pt as the counter electrode. To obtain monochromatic lights ranging from 400 to 670 nm, Xenon light was filtered through appropriate bandpass filters. The intensity of the light was measured using an ADCMT 8230E Optical Power Meter from ADC Corporation (Toyama, Japan). The measurement was conducted with an external bias of 1.0 V vs. NHE. The data parameters were collected and calculated according to Equation (1).

$$\text{IPCE (\%)} = \frac{I(\text{mA})}{P(\text{mW})} \times \frac{1240}{\lambda(\text{nm})} \times 100 \quad (3)$$

### 2.9. Theoretical Calculation

Theoretical energy levels were obtained using a B3LYP functional, which used the Stuttgart ECP (SDD) basis set for Ru and 6-31G\*\* for all the other atoms (C, H, O, N, P), calculated in a polarizable continuum model (PCM) of water using the Gaussian 09 package [48]. The molecular orbitals were visualized using the Gauss view 5.0.8 program.

## 3. Results and Discussion

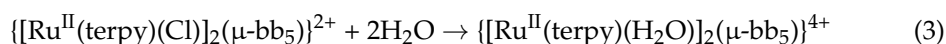
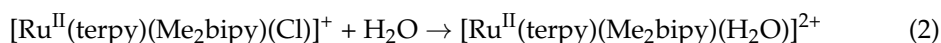
### 3.1. Synthesis and Characterizations

The synthesis of the precursor complexes  $[\text{Ru}(\text{terpy})(\text{Me}_2\text{bipy})(\text{Cl})]^+$  (1-Cl) and  $[\{\text{Ru}(\text{terpy})(\text{Cl})\}_2(\text{bb}_5)]^{2+}$  (2-Cl) followed the method reported previously [46,47]. The complexes were purified via silica gel column chromatography with methanol/acetone (2:1) as the eluent. The purity of the complexes was confirmed with  $^1\text{H}$  NMR, ESI mass spectrometry and an elemental analysis. The complexes  $[\text{Ru}(\text{terpy})(\text{Me}_2\text{bipy})(\text{H}_2\text{O})]^{2+}$  (1-H<sub>2</sub>O) and  $[\{\text{Ru}(\text{terpy})(\text{H}_2\text{O})\}_2(\text{bb}_5)]^{4+}$  (2-H<sub>2</sub>O) were generated in situ by irradiating 1-Cl and 2-Cl, respectively, in a pH 7 phosphate buffer (vide infra).

### 3.2. Photo-Induced Ligand Exchange

The absorption spectra of 1-Cl and 2-Cl in pure water exhibited absorptions that peaked at  $\lambda_{\max}$  486 nm ( $\epsilon = 8714 \text{ M}^{-1} \text{ cm}^{-1}$ ) and at  $\lambda_{\max}$  488 nm ( $\epsilon = 17,904 \text{ M}^{-1} \text{ cm}^{-1}$ ), respectively. These peaks were ascribed to the MLCT bands, which resulted from the transfer of charge from the metal to the ligand. Additionally, there were distinctive peaks observed at 314.5 and 315 nm for 1-Cl and 2-Cl, respectively, which were attributed to the ligand-based  $\pi-\pi^*$  transition. The molar extinction coefficient for 2-Cl was found to be twice that for 1-Cl, which was consistent with the “dinuclearity” present in 2-Cl.

The coordination chemistry of 1-Cl and 2-Cl featured a typical lability of the complexes because of the presence of the labile chlorido ligand, which can undergo aquation, accompanied by the blue-shift character of the absorption as it changed from  $\text{Ru}^{\text{II}}(\text{Cl})$  to  $\text{Ru}^{\text{II}}(\text{H}_2\text{O})$  [47]. While the ligand exchange could be triggered thermally [47] and through an acid treatment [49], in the present investigation, we observed that the aquation process could be generated through light irradiation (Equations (2) and (3)). As seen in Figure S1, the exposure of the water solution of 1-Cl and 2-Cl to visible light irradiation caused the movement of the MLCT band to  $\lambda_{\max}$  479 nm and to  $\lambda_{\max}$  480 nm, respectively, indicating the ligand exchange to aqua [47]. Additionally,  $^1\text{H}$ NMR monitoring showed the characteristic upfield shift in the C6 proton resonance following the light irradiation of 1-Cl and 2-Cl, as shown in Figures S11 and S12, indicating the formation of 1- $\text{H}_2\text{O}$  and 2- $\text{H}_2\text{O}$ , consistent with a previous report [47,50].



The TD-DFT calculations for 1-Cl, 1- $\text{H}_2\text{O}$ , 2-Cl and 2- $\text{H}_2\text{O}$  presented in Figure 2 showed that the ligand exchange from Cl to  $\text{H}_2\text{O}$  caused the stabilization of both the LUMO and HOMO of the metal complexes. Although the HOMO–LUMO gaps in the aqua complexes were slightly larger than the chlorido counterparts, as indicated by the experimental and calculated absorption maxima in Table S1, the exchange of Cl for  $\text{H}_2\text{O}$  appeared to be thermodynamically favorable due to the HOMO and LUMO stabilization.

### 3.3. Electrochemistry on nanoITO Surface

To examine the redox properties of the complexes, cyclic voltammetry (CV) experiments were conducted for 1-Cl and 2-Cl, and for the in situ-generated 1- $\text{H}_2\text{O}$  and 2- $\text{H}_2\text{O}$  in a three-electrode setup comprising of a nanoITO working electrode, a platinum counter electrode and a Ag/AgCl reference. Complexes 1-Cl and 2-Cl were dissolved in the pH 7.0 phosphate buffer and the CV was measured immediately. As illustrated in Figure 3, the mononuclear complex 1-Cl showed a reversible wave at the  $E_{1/2}$  0.86 V corresponding to the  $\text{Ru}^{\text{II}}(\text{Cl})/\text{Ru}^{\text{III}}(\text{Cl})$  redox cycle [43]. The measurement for 2-Cl observed only one redox wave at the  $E_{1/2}$  0.88 V assigned to  $(\text{Cl})\text{Ru}^{\text{II}}\text{-Ru}^{\text{II}}(\text{Cl})/(\text{Cl})\text{Ru}^{\text{III}}\text{-Ru}^{\text{III}}(\text{Cl})$ , despite having two metal centers. The concentration of the 2-Cl solution in the buffer was half that of the mononuclear 1-Cl, and the CV data revealed that they had the same current height, as seen in Figure 3. This result indicated that the single redox wave in 2-Cl contained two sets of the one-electron process originating from two identical metal centers. The identical redox character of the two coordination sites was evident from the HOMO surface plots in trans-trans-2-Cl and in cis-cis-2-Cl (Figure 2), which suggested that each coordination site in the dinuclear chloride complex possessed an identical electron distribution.

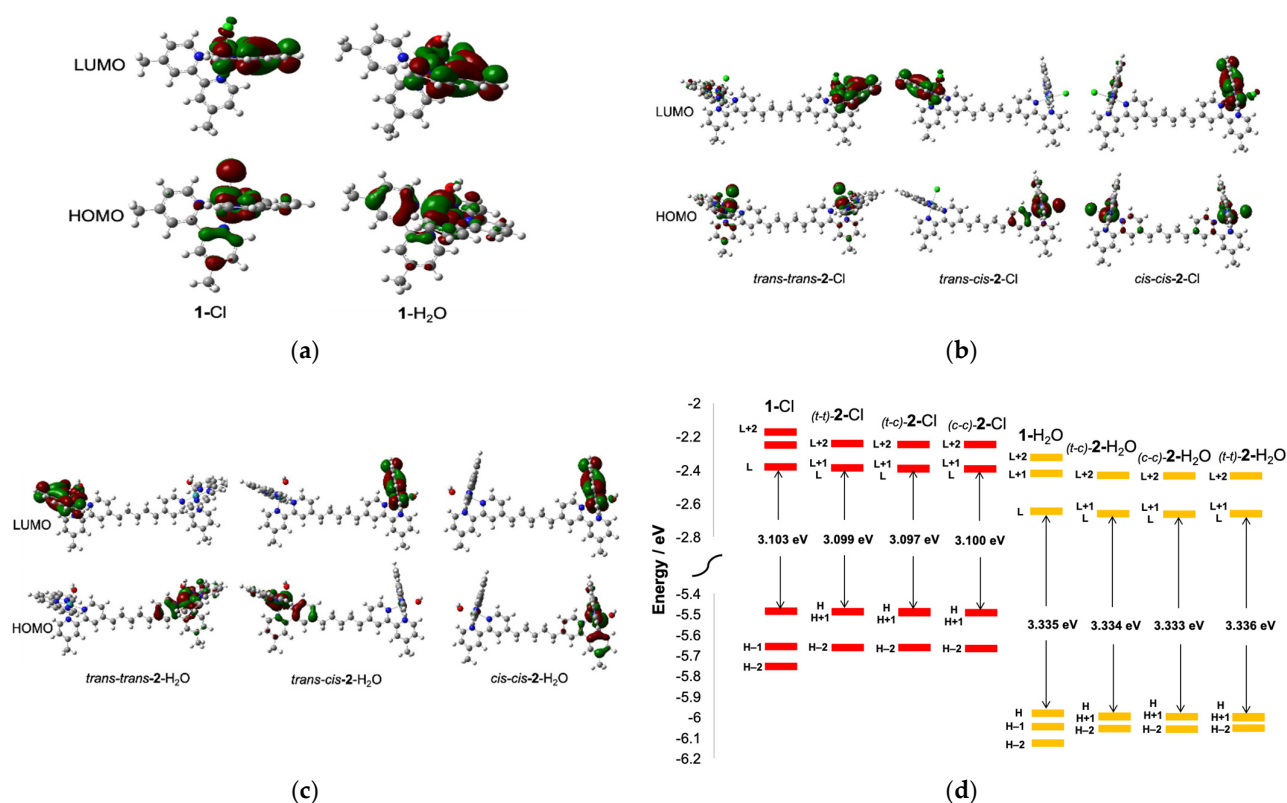


**Figure 2.** (a) The HOMO and LUMO surface plots of 1-Cl and 1-H<sub>2</sub>O; (b) the HOMO and LUMO surface plots of trans-trans-2-Cl, trans-cis-2-Cl and cis-cis-2-Cl; (c) the HOMO and LUMO surface plots of trans-trans-2-H<sub>2</sub>O, trans-cis-2-H<sub>2</sub>O and cis-cis-2-H<sub>2</sub>O; (d) HOMO and LUMO energies of all geometric isomers of 2-Cl and 2-H<sub>2</sub>O, showing the stabilization of both HOMO and LUMO following the formation of the aqua forms, although there was an apparent increase in the HOMO–LUMO energy gap consistent with the experimental electronic absorption presented in Table S1.

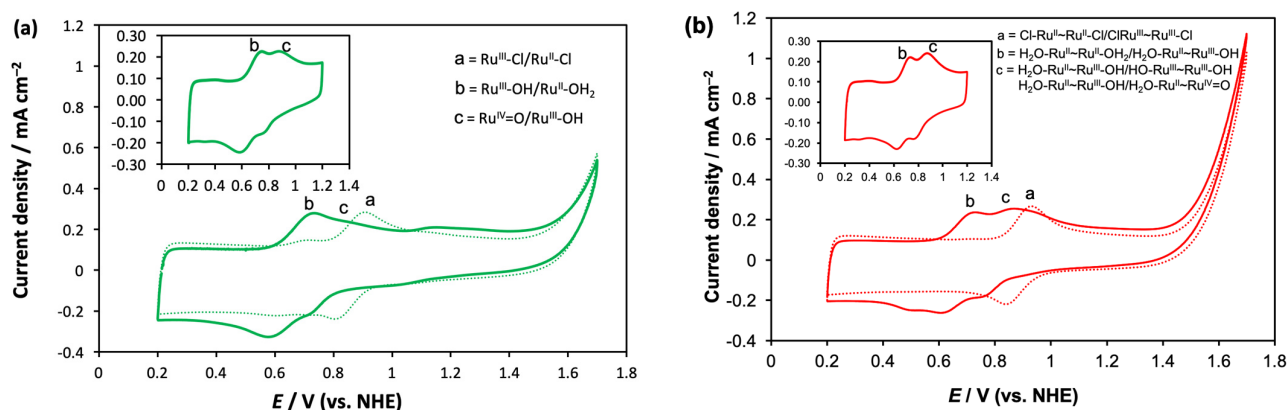


**Figure 3.** (a) The CV of 1-Cl (dotted line) and the photo-generated 1-H<sub>2</sub>O (solid line); (b) the CV of 2-Cl (dotted line) and 2-H<sub>2</sub>O (solid line). The electrochemical measurements were carried out using a three-electrode system with *nanoITO* screen-printed on FTO as working electrode, Ag/AgCl as the reference electrode and Pt as the counter electrode. Complexes 1-Cl (0.2 mM) and 2-Cl (0.1 mM) were dissolved in pH 7 phosphate buffer. Complexes 1-H<sub>2</sub>O and 2-H<sub>2</sub>O were generated in situ by exposing the chloride complex solutions to Xenon light (160 mW cm<sup>-2</sup>) for 15 min. The scan rate used in all cases was 100 mV s<sup>-1</sup>.

Complexes 1-H<sub>2</sub>O and 2-H<sub>2</sub>O were generated in situ by irradiating 1-Cl and 2-Cl solutions in the pH 7 phosphate buffer, respectively, for 15 min. Figure 3a displays the CV of 1-H<sub>2</sub>O, which exhibited two one-electron redox cycles at 0.67 V and 0.82 V, respectively. These cycles were attributed to the proton-coupled electron transfer (PCET) processes Ru<sup>II</sup>(H<sub>2</sub>O)/Ru<sup>III</sup>(OH) and Ru<sup>III</sup>(OH)/Ru<sup>IV</sup>=O, respectively [49]. These results confirmed the photo-induced aquation process, which was consistent with the UV-Vis and <sup>1</sup>HNMR observations described earlier. The pH-dependent PCET and evidence of one-electron oxidation of Ru<sup>II</sup>(H<sub>2</sub>O) to Ru<sup>III</sup>(OH) in neutral pH was reported on previously [51,52]. In contrast to 1-H<sub>2</sub>O, the CV of the in situ-generated aqua complex 2-H<sub>2</sub>O exhibited multiple cathodic peaks that were clearly identified when scanned from 0.2 to 1.6 V, although the forward anodic scan showed only two distinctive peaks (Figure 3b). While the CV scan from 0.2 to 1.2 V featured two well-defined redox cycles (inset of Figure 3b), the presence of the multiple cathodic peaks after the forward anodic scan to 1.6 V indicated the accumulation of higher oxidation 2-H<sub>2</sub>O states on the *nano*ITO surface beyond 1.2 V. This provided evidence of the stepwise one-electron PCETs in 2-H<sub>2</sub>O. Moreover, unlike 2-Cl, the HOMO surface plots of all the geometric isomers of 2-H<sub>2</sub>O exhibited a nonidentical electron distribution pattern of the two coordination sites (Figure 2c). This strongly suggests that each site possesses different redox behavior. As a result, the two redox cycles noticed for 2-H<sub>2</sub>O were assigned as a stepwise one-electron oxidation: (H<sub>2</sub>O)Ru<sup>II</sup>-Ru<sup>II</sup>(OH<sub>2</sub>)/(H<sub>2</sub>O)Ru<sup>II</sup>-Ru<sup>III</sup>(OH) (0.68 V) and (H<sub>2</sub>O)Ru<sup>II</sup>-Ru<sup>III</sup>(OH)/(HO)Ru<sup>III</sup>-Ru<sup>III</sup>(OH) (0.82 V). Consistent with the PCET via hydrogen bonding in the dinuclear ruthenium complexes bridged by a nonflexible linker [52], in the current study, 2-H<sub>2</sub>O was proposed to feature a hydrogen-bonded PCET, because the flexibility of the alkyl bridge would allow for the orientation of the two coordination sites to be optimal for hydrogen bonding, as demonstrated in Figure 4. The complete assignments of the redox potentials of each complex are presented in Table 1.

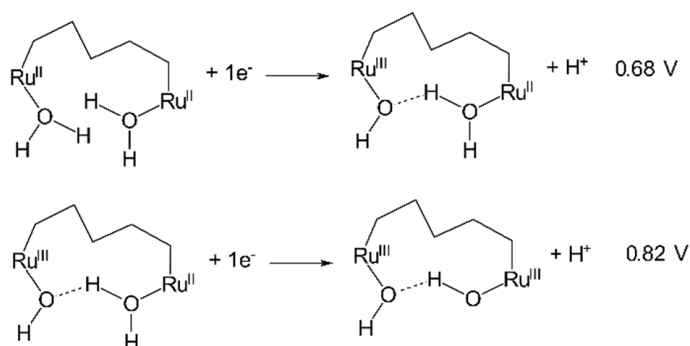


**Figure 4.** The proposed PCET in 2-H<sub>2</sub>O showing the (H<sub>2</sub>O)Ru<sup>II</sup>-Ru<sup>II</sup>(OH<sub>2</sub>)/(H<sub>2</sub>O)Ru<sup>II</sup>-Ru<sup>III</sup>(OH) at 0.68 V and (H<sub>2</sub>O)Ru<sup>II</sup>-Ru<sup>III</sup>(OH)/(HO)Ru<sup>III</sup>-Ru<sup>III</sup>(OH) at 0.82 V. The flexibility of the alkyl bridging ligand is predicted to facilitate the interaction of the two metal centers through hydrogen bonding.

**Table 1.** The assignments of the redox potentials of 1-Cl and 2-Cl and those of the photo-generated 1-H<sub>2</sub>O and 2-H<sub>2</sub>O observed on *nano*ITO surface. The measurements were performed in 0.1 M pH 7 phosphate buffer. The in situ generation of the aqua complexes was carried out by irradiating the complex solutions for 15 min. All the potential values were relative to NHE.  $E_{\frac{1}{2}} = |E_{pa} - E_{pc}| / 2$ .  $\Delta E = E_{pa} - E_{pc}$  in mV.

Complex	Assignment	$E_{pa}$ (V)	$E_{pc}$ (V)	$E_{\frac{1}{2}}$ (V)	$\Delta E$ (mV)
1-Cl	Ru <sup>II</sup> -Cl/Ru <sup>III</sup> -Cl	0.90	0.81	0.86	90
1-H <sub>2</sub> O	Ru <sup>II</sup> (OH <sub>2</sub> )/Ru <sup>III</sup> (OH)	0.74	0.60	0.67	140
1-H <sub>2</sub> O	Ru <sup>III</sup> (OH)/Ru <sup>IV</sup> =O	0.88	0.76	0.82	120
2-Cl	(Cl)Ru <sup>II</sup> -Ru <sup>II</sup> (Cl)/(Cl)Ru <sup>III</sup> -Ru <sup>III</sup> (Cl)	0.92	0.84	0.88	80
2-H <sub>2</sub> O	(H <sub>2</sub> O)Ru <sup>II</sup> -Ru <sup>II</sup> (-OH <sub>2</sub> )/(HO)Ru <sup>III</sup> -Ru <sup>II</sup> (OH <sub>2</sub> )	0.73	0.62	0.68	110
2-H <sub>2</sub> O	(HO)Ru <sup>III</sup> -Ru <sup>II</sup> (OH <sub>2</sub> )/(HO)Ru <sup>III</sup> -Ru <sup>III</sup> (OH)	0.87	0.77	0.82	100

### 3.4. Photo-Electrochemistry on nanoITO Surface

The linear scan voltammetry (LSV) tests were carried out in the range 0.2–1.6 V under visible light irradiation to explore the photocurrent responses of the aqua complexes in the buffer solution on the surface of *nano*ITOs, with the data shown in Figure 5a. The  $J$ - $V$  curve for the *nano*ITOs in the buffer only in the absence of light irradiation demonstrated that the onset of water oxidation occurred at a 1.5 V applied potential, or 680 mV overpotential. In stark contrast, under visible light irradiation, the  $J$ - $V$  curve for the *nano*ITOs showed a much earlier onset at 0.9 V or 83 mV overpotential. The lower amount of overpotential under light irradiation indicated that *nano*ITOs can absorb photon energy to create a hole–electron separation at an applied bias to facilitate water oxidation on the surface. The LSV under light irradiation carried out for the *nano*ITOs in the presence of 1-H<sub>2</sub>O and 2-H<sub>2</sub>O also revealed a lower onset potential, which was characterized by an apparent increase in the photocurrent in the potential range 0.6–1.3 V, where PCET occurred.

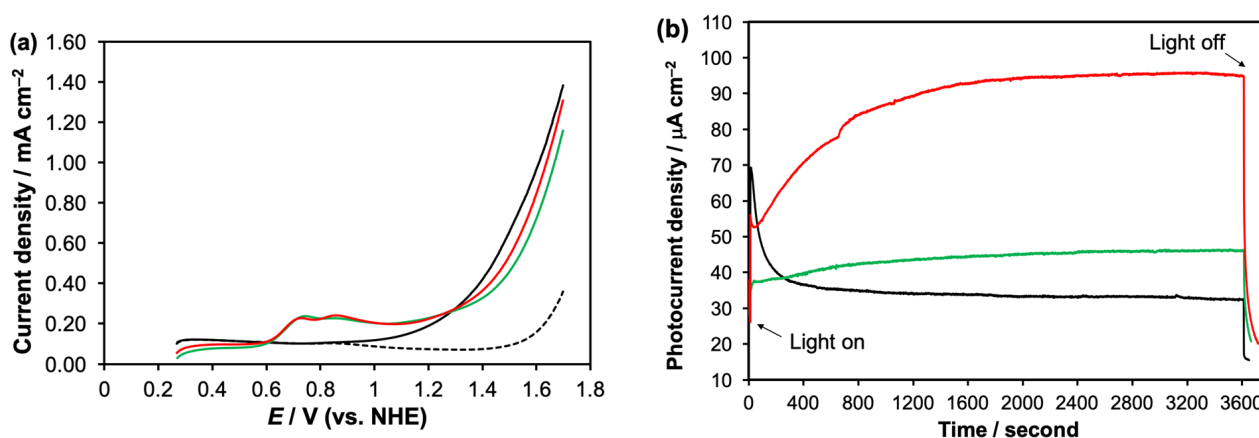


**Figure 5.** (a) The  $J$ - $V$  curves of *nano*ITOs in phosphate buffer without light irradiation (dashed line), *nano*ITO under visible light irradiation (black solid line), *nano*ITO in the presence of 1-H<sub>2</sub>O (green) and *nano*ITO in the presence of 2-H<sub>2</sub>O (red) performed under light irradiation; (b) the  $J$ - $t$  curves for *nano*ITO in buffer-only (black), in the presence of 1-H<sub>2</sub>O (green) and in the presence of 2-H<sub>2</sub>O (red) obtained under on-off Xenon light irradiation (160 mW cm<sup>-2</sup>) held at 1.0 V for a period of 3600 s.

Based on the LSV results, the photolysis experiments were then performed at a potential of 1.0 V for a duration 3600 s, with the data presented in Figure 5b. In buffer only, the *nano*ITOs gave a photocurrent spike at 70 A cm<sup>-2</sup>, which dropped quickly to the steady-state current of 33 A cm<sup>-2</sup> due to the fast electron–hole recombination. The presence of 1-H<sub>2</sub>O in the solution gave the lower photocurrent spike, but a higher and more persistent steady-state current at 40 A cm<sup>-2</sup>. In contrast to the buffer-only and 1-H<sub>2</sub>O experiments, the photolysis experiment in the presence of 2-H<sub>2</sub>O exhibited a progressive increase in the photocurrent for 1200 s before leveling off at 95 A cm<sup>-2</sup>. Although no oxygen gas was detected by the oxygen sensor, the buffer-only produced 0.20 μmol H<sub>2</sub>, while 1-H<sub>2</sub>O and 2-H<sub>2</sub>O generated 0.23 μmol and 0.70 μmol hydrogen gas, respectively.

The curve-shaped photocurrent response shown by 2-H<sub>2</sub>O that was significantly higher than the other two systems was indicative of the chemical processes unique to the dinuclear complex occurring during the photolysis on the surface of the *nano*ITOs. Our SEM investigation of the *nano*ITO surface after the photolysis in the presence of 2-H<sub>2</sub>O revealed the deposited microparticle, as shown in Figure 6b(1). While no deposition occurred for 1-H<sub>2</sub>O (Figure 6b(2)), the greater photocurrent by 2-H<sub>2</sub>O must have, therefore, been caused exclusively by the photo-electrochemical process involving the accessible redox states of the dinuclear complex. The CV analysis of the deposited product in the phosphate buffer (Figure 6a) showed two redox cycles at  $E_{1/2}$  0.82 V and 1.28 V, which were assigned to the (H<sub>2</sub>O)Ru<sup>II</sup>-Ru<sup>III</sup>(OH)/(HO)Ru<sup>III</sup>-Ru<sup>III</sup>(OH) and (HO)Ru<sup>III</sup>-Ru<sup>III</sup>(OH)/(HO)Ru<sup>III</sup>-Ru<sup>IV</sup>(O) redox events, respectively. Therefore, we sus-

pected that the deposited product was the dinuclear complex in its oxidized  $(\text{H}_2\text{O})\text{Ru}^{\text{II}}-\text{Ru}^{\text{III}}(\text{OH})$  form that accumulated on the *nanoITO* surface. As seen in Figure 6a, although the first CV cycle of the deposited complex displayed two distinctive redox cycles, the current height belonging to  $(\text{HO})\text{Ru}^{\text{III}}-\text{Ru}^{\text{III}}(\text{OH})/(\text{HO})\text{Ru}^{\text{III}}-\text{Ru}^{\text{IV}}(\text{O})$  gradually decreased as further cycles proceeded, accompanying the appearance of the  $(\text{H}_2\text{O})\text{Ru}^{\text{II}}-\text{Ru}^{\text{II}}(\text{OH}_2)/(\text{H}_2\text{O})\text{Ru}^{\text{II}}-\text{Ru}^{\text{III}}(\text{OH})$  redox. Therefore, during the multiple CV scans, the complex returned to its  $(\text{H}_2\text{O})\text{Ru}^{\text{II}}-\text{Ru}^{\text{II}}(\text{OH}_2)$  state. The decrease in the current heights after multiple scans was possibly due to the dissolution of the deposited microparticle in the buffer solution. The XPS spectrum of the deposited product on the *nanoITOs* (Figure 6c) showed the presence of Ru 3d 3/2, Ru 3d 5/2, C 1 s, O 1 s and N 1 s at binding energies 298, 285, 285, 533 and 402 eV, respectively [53], which further confirmed the deposition of the dinuclear complex molecule on the surface.

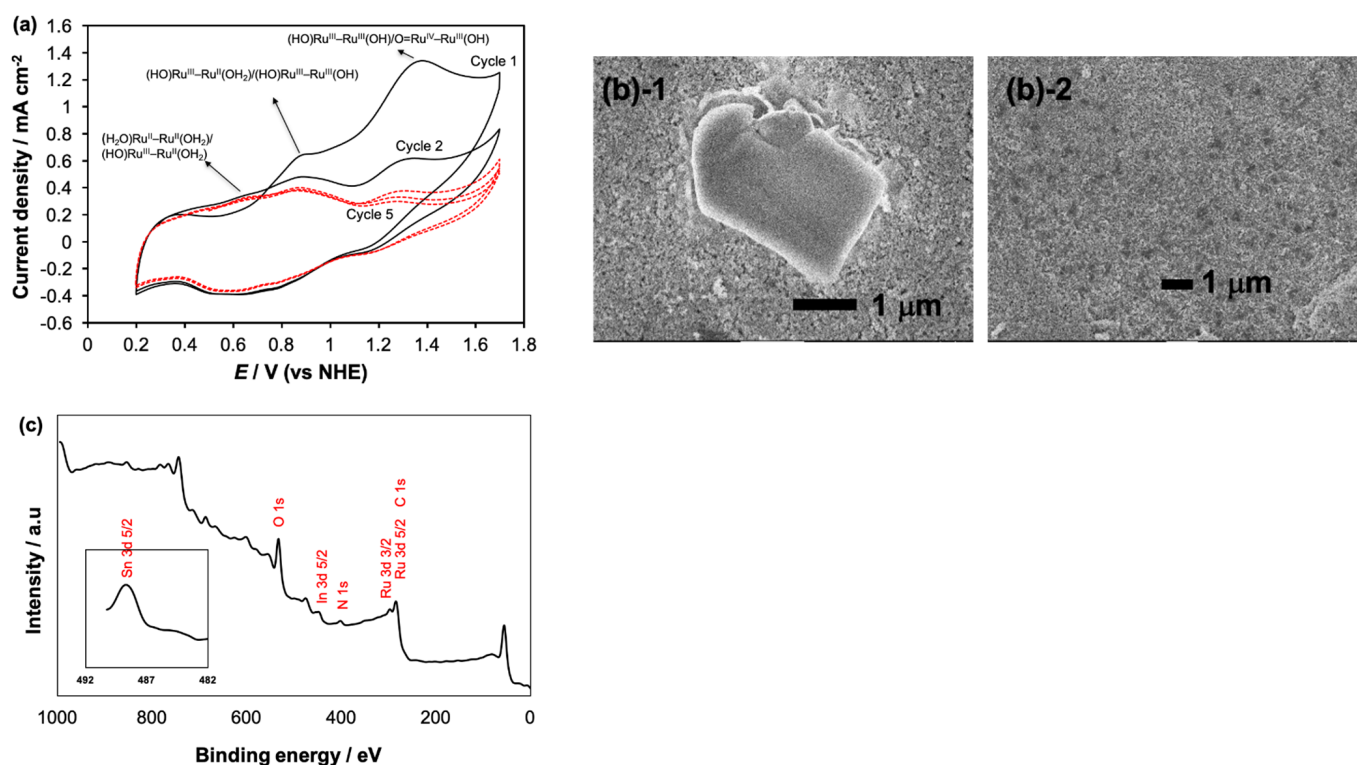


**Figure 6.** (a) The cyclic voltammogram of the deposited product obtained after the photolysis of 2- $\text{H}_2\text{O}$ . The *nanoITO* working electrode that contained the deposited product was taken out and rinsed and the CV was performed in pH 7.0 phosphate buffer; (b(1)) the SEM image of the *nanoITO* obtained after the photolysis of 2- $\text{H}_2\text{O}$ , showing the deposited microparticle believed to be the stable oxidized form of  $(\text{H}_2\text{O})\text{Ru}^{\text{II}}-\text{Ru}^{\text{III}}(\text{OH})$  in comparison with the SEM image of *nanoITOs* after photolysis of 1- $\text{H}_2\text{O}$  (b(2)), which showed no deposition; (c) the XPS spectrum of the *nanoITOs* containing the deposited product after the photolysis of 2- $\text{H}_2\text{O}$ , showing Ru 3d 3/2, Ru 3d 5/2, C 1 s, O 1 s and N 1 s peaks.

### 3.5. Plausible Photo-Electrochemical Mechanism

We conducted the incident photon to current efficiency (IPCE) spectroscopy and spectro-electrochemistry studies of buffer-only, 1- $\text{H}_2\text{O}$  and 2- $\text{H}_2\text{O}$  solutions to corroborate the photo-electrochemical mechanism in the three systems. As shown in Figure 7, the IPCE spectra of the *nanoITOs* in a buffer-only system at a potential of 1.0 V were consistent with its absorption spectrum at the same potential (Figure S5), which indicated that the photon-to-current conversion through *nanoITOs* occurred primarily in the UV region. In contrast to the *nanoITOs* in buffer only, the IPCE measurements for *nanoITOs* in 1- $\text{H}_2\text{O}$  and 2- $\text{H}_2\text{O}$  showed typical peaks at approximately 450 nm and considerable photon conversion

beyond 500 nm, which clearly resembled the absorption spectra of the corresponding complexes (see Figures S6 and S7). The resemblance of the IPCE of 1-H<sub>2</sub>O and 2-H<sub>2</sub>O with their absorption spectra confirmed that the complex molecules absorbed the photon energy in the visible region and converted it to a current via electron injection into the conduction band of the *nano*ITOs. Although the %IPCE was very low, the higher value observed for 2-H<sub>2</sub>O in comparison to 1-H<sub>2</sub>O indicated the better photon-to-current conversion by the dinuclear complex, which was consistent with the photolysis data (Figure 5b).

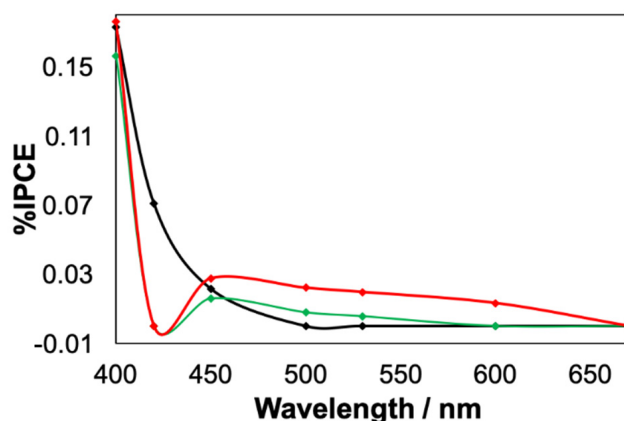


**Figure 7.** The IPCE spectra of *nano*ITOs in buffer only (black), in the presence of 1-H<sub>2</sub>O (green) and in the presence of 2-H<sub>2</sub>O (red) performed at 1.0 V.

Figure 8 shows the redox state regions of 1-H<sub>2</sub>O and 2-H<sub>2</sub>O derived from the spectro-electrochemistry experiments performed in the range 0.2–1.7 V (see Figures S5–S7). A close inspection of the absorbance changes in the MLCT band plotted against the applied potential for 1-H<sub>2</sub>O revealed the presence of three regions corresponding to Ru<sup>II</sup>(OH<sub>2</sub>), Ru<sup>III</sup>(OH) and Ru<sup>IV</sup>(O), while 2-H<sub>2</sub>O displayed four distinctive regions belonging to (H<sub>2</sub>O)Ru<sup>II</sup>–Ru<sup>II</sup>(OH<sub>2</sub>), (H<sub>2</sub>O)Ru<sup>II</sup>–Ru<sup>III</sup>(OH), (HO)Ru<sup>III</sup>–Ru<sup>III</sup>(OH) and (HO)Ru<sup>III</sup>–Ru<sup>IV</sup>(O), which confirmed the stepwise one-electron PCET in 2-H<sub>2</sub>O.

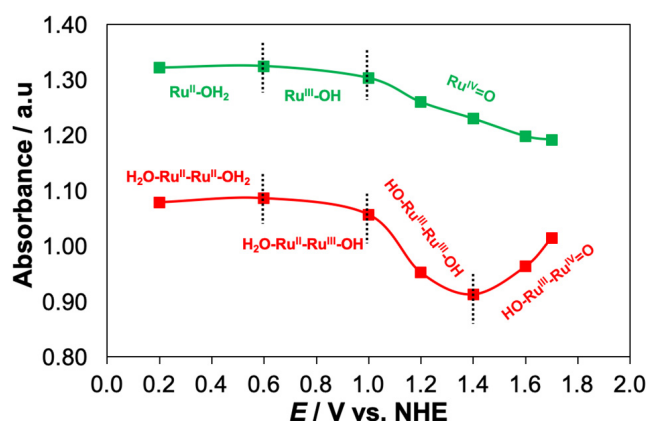


**Figure 8.** The redox state regions of 1-H<sub>2</sub>O (green) and 2-H<sub>2</sub>O (red) obtained from the plots of the absorbance change in the MLCT band in response to the changing potentials.

The spectro-electrochemistry measurements also revealed that increasing the applied potential to 1.0 V for both 1-H<sub>2</sub>O and 2-H<sub>2</sub>O resulted in only a slight decrease in the MLCT band (Figures S6 and S7), suggesting the dominant Ru<sup>II</sup>(H<sub>2</sub>O) and (H<sub>2</sub>O)Ru<sup>II</sup>–Ru<sup>II</sup>(OH<sub>2</sub>) species existing on the surface of the *nano*ITOs. During a bulk electrolysis or a chemical oxidation of Ru<sup>II</sup>(OH<sub>2</sub>), the MLCT band completely disappeared as it underwent oxidation to Ru<sup>III</sup>(OH) and further to Ru<sup>IV</sup>(O) [50]. In this investigation, the slight decrease in the

MLCT band intensity during the photolysis experiments inferred that the visible-light-absorbing species  $\text{Ru}^{\text{II}}(\text{H}_2\text{O})$  of 1- $\text{H}_2\text{O}$  and  $(\text{H}_2\text{O})\text{Ru}^{\text{II}}\text{-Ru}^{\text{II}}(\text{OH}_2)$  of 2- $\text{H}_2\text{O}$  existed in the solution–metal-oxide interface.

In the buffer-only system (Figure 9), the absorption of the photon energy by the *nano*ITOs caused hole–electron separation in the semiconductor. The photocurrent declined rapidly, because the electron recombined easily with the hole. The generated photocurrent during the photolysis was low and was not sufficient to drive the oxidation of the water molecules to oxygen.

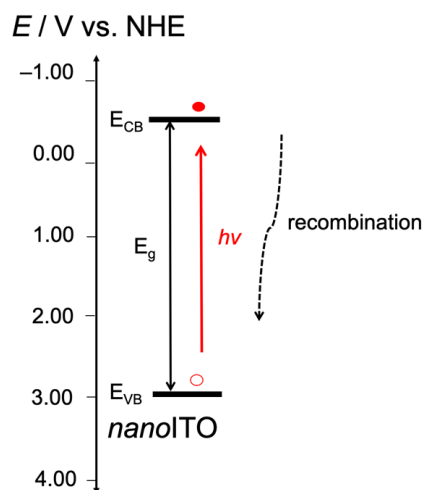


**Figure 9.** The proposed energy diagram for the photo-electrochemical process following the light absorption by *nano*ITOs in buffer-only system performed at 1.0 V. The electron–hole separation that occurred in competition with electron recombination, leading to the sharp decline in the photocurrent, as shown in Figure 5b. The *nano*ITO conduction band ( $E_{\text{CB}}$ )  $-0.77$  V SCE or equal to  $-0.53$  V NHE followed that reported previously [40]. The band gap energy ( $E_g$ )  $+3.45$  eV was estimated from the Tauc plot derived from the UV–visible spectrum at 1.0 V, as given in Figure S8.

In the presence of 1- $\text{H}_2\text{O}$ , the higher photocurrent spike and the improved steady-state photocurrent were due to the hole being used to oxidize the mononuclear ruthenium complex in the solution–metal-oxide interface, which, therefore, prevented electron/hole recombination. Given that the potentials of  $\text{Ru}^{\text{II}}(\text{OH}_2)/\text{Ru}^{\text{III}}(\text{OH})$  ( $+0.67$  V) and  $\text{Ru}^{\text{III}}(\text{OH})/\text{Ru}^{\text{IV}}=\text{O}$  ( $+0.82$  V) were lower than the  $E_{\text{VB}}$  of the *nano*ITOs, the hole extraction by both  $\text{Ru}^{\text{II}}(\text{H}_2\text{O})$  and  $\text{Ru}^{\text{III}}(\text{OH})$  was thermodynamically preferable. As inferred from Figure 7, the IPCE spectrum of the *nano*ITOs in the presence of 1- $\text{H}_2\text{O}$  indicated that  $\text{Ru}^{\text{II}}(\text{OH}_2)$  could absorb the photon energy at the visible region, which caused the excitation of the molecule and the subsequent electron injection into the conduction band of the *nano*ITOs. This process could have occurred because the  $\text{Ru}^{\text{II}*}(\text{OH}_2)/\text{Ru}^{\text{III}}(\text{OH})$  excited-state potential ( $-1.45$  V) was more negative than that of the  $E_{\text{CB}}$  of the *nano*ITOs.

In a similar manner, in the presence of 2- $\text{H}_2\text{O}$ , the hole could be transferred to  $(\text{H}_2\text{O})\text{Ru}^{\text{II}}\text{-Ru}^{\text{II}}(\text{OH}_2)$  and to  $(\text{H}_2\text{O})\text{Ru}^{\text{II}}\text{-Ru}^{\text{III}}(\text{OH})$  to yield the respective higher-oxidation state complexes, as presented in Figure 10c. The one-electron redox processes  $(\text{H}_2\text{O})\text{Ru}^{\text{II}}\text{-Ru}^{\text{II}}(\text{OH}_2)/(\text{H}_2\text{O})\text{Ru}^{\text{II}}\text{-Ru}^{\text{III}}(\text{OH})$  and  $(\text{H}_2\text{O})\text{Ru}^{\text{II}}\text{-Ru}^{\text{III}}(\text{OH})/(\text{HO})\text{Ru}^{\text{III}}\text{-Ru}^{\text{III}}(\text{OH})$ , which occurred at 0.68 V and 0.82 V, respectively, were lower than the  $E_{\text{VB}}$  of the *nano*ITOs, thus, allowing the hole transfer to take place. The IPCE spectrum given in Figure 7 (red trace) also indicating that the dinuclear species  $(\text{H}_2\text{O})\text{Ru}^{\text{II}}\text{-Ru}^{\text{II}}(\text{OH}_2)$  absorbed photon energy in the visible region, which caused its excitation to  $(\text{H}_2\text{O})\text{Ru}^{\text{II}}\text{-Ru}^{\text{II}*}(\text{OH}_2)$  and the subsequent electron injection into the conduction band of the *nano*ITOs. Such an electron injection could occur because the  $(\text{H}_2\text{O})\text{Ru}^{\text{II}}\text{-Ru}^{\text{II}*}(\text{OH}_2)/(\text{H}_2\text{O})\text{Ru}^{\text{II}}\text{-Ru}^{\text{III}}(\text{OH})$  excited potential ( $-1.42$  V) was more negative in comparison with the  $E_{\text{CB}}$  of the *nano*ITOs.

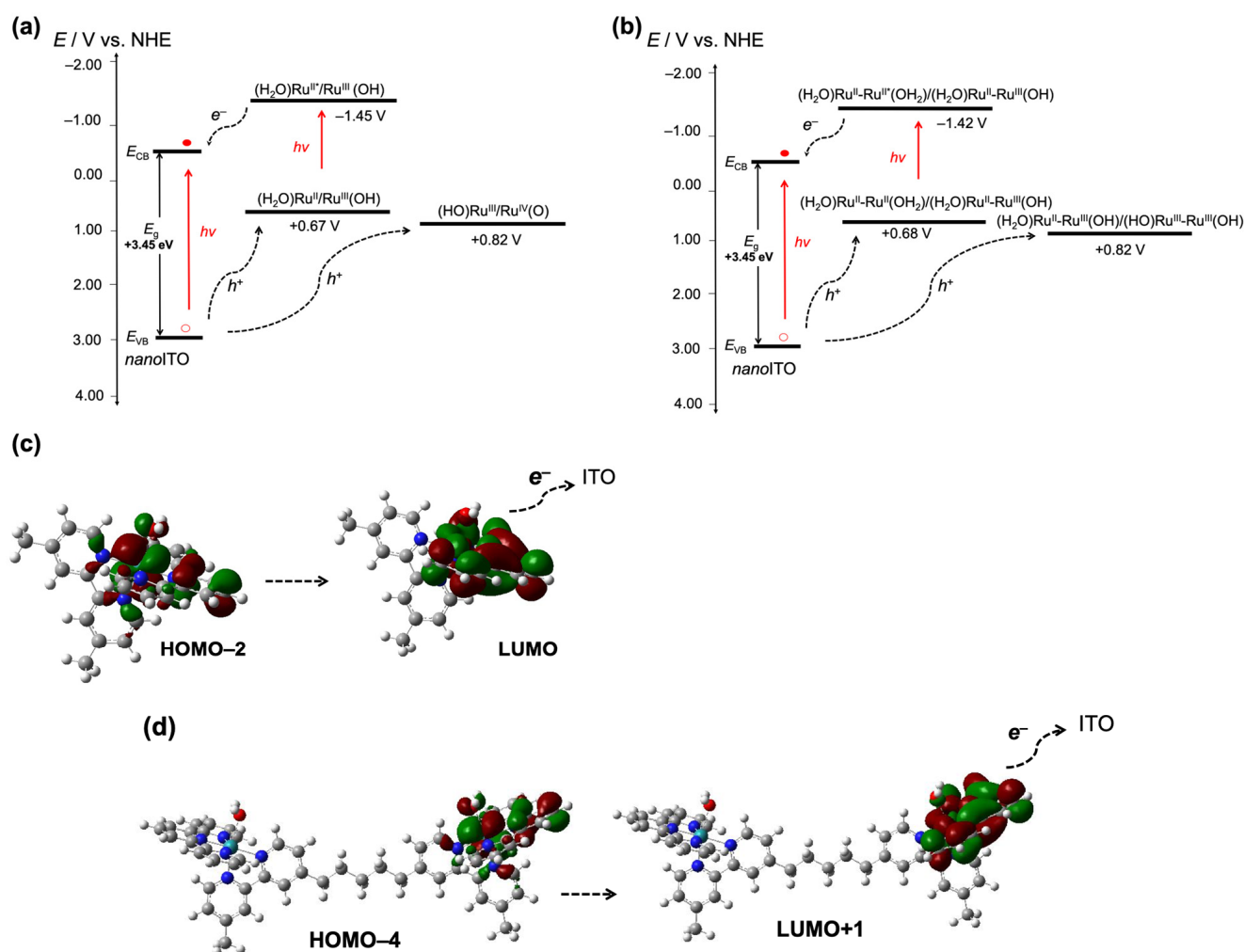


**Figure 10.** (a) The proposed energy diagram representing the photo-electrochemical processes occurring on *nanoITOs* in the presence of 1- $H_2O$  during the photolysis at 1.0 V. The created hole was extracted through  $Ru^{II}(OH_2)$  to form  $Ru^{III}(OH)$  then  $Ru^{IV}(O)$ . The visible light absorption using  $Ru^{II}(OH_2)$  caused its excitation and subsequent electron injection to form  $Ru^{III}(OH)$ ; (b) the proposed energy diagram representing the photo-electrochemical processes occurring on *nanoITOs* in the presence of 2- $H_2O$  during the photolysis at 1.0 V. The created hole was extracted through  $(H_2O)Ru^{II}-Ru^{II}(OH_2)$  to form  $(H_2O)Ru^{II}-Ru^{III}(OH)$  then  $(HO)Ru^{III}-Ru^{III}(OH)$ . The visible light absorption using  $(H_2O)Ru^{II}-Ru^{II}(OH_2)$  caused its excitation and subsequent electron injection to form  $(H_2O)Ru^{II}-Ru^{III}(OH)$ . The ground-state potentials were determined from the CV data, while the excited-state potentials were determined from the equation  $E^{*/+} = E^0(Ru^{II}/Ru^{III}) - E_{0-0}$  [54,55], where  $E_{0-0}$  was obtained from the intersection between absorption and emission (Figure S9). The *nanoITO* conduction band ( $E_{CB}$ )  $-0.77$  V SCE or equal to  $-0.53$  V NHE followed that reported previously [40]. The band gap energy ( $E_g$ )  $+3.45$  eV was estimated from the Tauc plot derived from the UV-visible spectrum at 1.0 V as given in Figure S8. [47]; (c) the surface plots of the dominant H-2  $\rightarrow$  L transition in 1- $H_2O$  showing the electron distribution in terpyridine and  $H_2O$  ligands of the L state; (d) the surface plots of the dominant H-4  $\rightarrow$  L+1 transition in 2- $H_2O$  (trans-trans isomer) showing the electron distribution in terpyridine and  $H_2O$  ligands of the L+1 state.

The above energetics data were consistent with the previous study, which reported that electron injection by the surface-bound ruthenium complexes into ITO nanoparticles was bias-dependent, and was due to the overlap between the conduction band of the nanoparticles and the  $Ru^{III}/Ru^{II*}$  energy [43]. In the present investigation, the very low IPCE values observed for both 1- $H_2O$  and 2- $H_2O$  suggested that the formation of the

respective oxidized products through this photo-electrochemical process did not occur effectively. One possible cause was the ineffective electron injection into the *nanoITO* conduction band in the solution–metal-oxide interface because of the lack of an anchoring group or binding unit, such as carboxylic acid or phosphonic acid, which would otherwise facilitate a better electron injection [40–43]. Nevertheless, the dominant H-2 → L transition in the 1-H<sub>2</sub>O and H-4 → L + 1 transition in 2-H<sub>2</sub>O rendered the characteristic metal-to-ligand transition in both complexes, where the electron of the LUMO states of both molecules was localized in the terpyridine and aqua (H<sub>2</sub>O) ligands (Figure 10c,d). Thus, although the binding unit to *nanoITO* was absent, the accumulation of electrons in the terpyridine and H<sub>2</sub>O ligands of the excited states of the molecules suggested a possible electron injection through these moieties. The superior steady-state photocurrent shown by 2-H<sub>2</sub>O associated with the accumulation of the stable photo-oxidized product (H<sub>2</sub>O)Ru<sup>II</sup>–Ru<sup>III</sup>(OH) proves that the photo-electrochemical properties of the ruthenium complexes in the solution–metal-oxide interface was structure-dependent. Although the electron injection capacity of both complexes was energetically favorable, the photo-electrochemical enhancement shown by 2-H<sub>2</sub>O was the likely consequence of its structure. The two coordination sites in 2-H<sub>2</sub>O possessed different redox characters that were bridged by a flexible alkyl chain, which may have caused a “chelating effect” that directed the orientation of the –OH- and –H<sub>2</sub>O-rich coordination sites towards the metal oxide through hydrogen bonding as shown in Figure 11. While the “chelating effect” was absent in 1-H<sub>2</sub>O, through this effect, 2-H<sub>2</sub>O molecules in the solution interacted better with the *nanoITO* surface, which led to the facile photodeposition of the oxidized form of the molecule on the surface of the metal oxide.

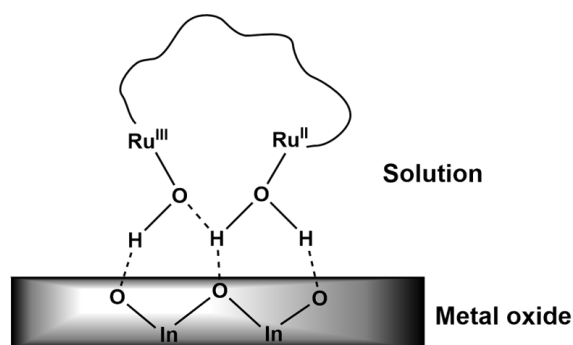


**Figure 11.** A diagram of the proposed “chelating effect” depicting the interaction between the two coordination sites of 2-H<sub>2</sub>O with the metal oxide of *nanoITO*. The terpyridine ligand and the bipyridine of the bb<sub>5</sub> bridging ligand were omitted for clarity.

#### 4. Conclusions

We demonstrated for the first time the photo-induced ligand exchange in 1-Cl and 2-Cl to yield the corresponding aqua complexes 1-H<sub>2</sub>O and 2-H<sub>2</sub>O, as monitored by UV–Vis, <sup>1</sup>HNMR and photoluminescence spectroscopies. In the buffer-only system, the *nanoITO* showed a rapid photocurrent decay because of the characteristic electron–hole recombination. In the presence of the in situ-generated 1-H<sub>2</sub>O and 2-H<sub>2</sub>O, the photocurrents held at 1.0 V were higher and steadier, which demonstrated the hole extraction through the complex molecules, therefore, inhibiting electron recombination. The IPCE data for both 1-H<sub>2</sub>O and 2-H<sub>2</sub>O on the *nanoITOs* revealed the photon-to-electron conversion in the visible region, because the excitation of the complex molecules facilitated the electron injection into the conduction band of the *nanoITOs*. Compared with 1-H<sub>2</sub>O, the more superior photo-electrochemical response and the higher IPCE and hydrogen production shown by 2-H<sub>2</sub>O were associated with the accumulation of the photo-oxidized product (H<sub>2</sub>O)Ru<sup>II</sup>–Ru<sup>III</sup>(OH), which proved that the photo-electrochemistry of the ruthenium complexes in the solution–metal-oxide interface was structure-dependent.

**Supplementary Materials:** The following supporting information can be downloaded at: <https://www.mdpi.com/article/10.3390/pr11072060/s1>, Table S1: TD-DFT data for 1-Cl, 1-H<sub>2</sub>O, 2-Cl and 2-H<sub>2</sub>O; Figure S1: time-course UV-Vis spectra of 1-Cl during light irradiation; Figure S2: time-course UV-Vis spectra of 2-Cl during light irradiation; Figure S3: photoluminescence spectra for 1-Cl and 1-H<sub>2</sub>O; Figure S4: photoluminescence spectra for 2-Cl and 2-H<sub>2</sub>O; Figure S5: the absorption spectra of *nano*ITO in varying potentials; Figure S6: the absorption spectra of 1-H<sub>2</sub>O on *nano*ITO in varying potentials; Figure S7: the absorption spectra of 2-H<sub>2</sub>O on *nano*ITO in varying potentials; Figure S8: Tauc plot of *nano*ITO at 1.0 V; Figure S9:  $E_{0-0}$  value of 1-H<sub>2</sub>O; Figure S10:  $E_{0-0}$  value of 1-H<sub>2</sub>O; Figure S11: <sup>1</sup>H NMR spectra of 1-Cl and 1-H<sub>2</sub>O; Figure S12: <sup>1</sup>H NMR spectra of 2-Cl and 2-H<sub>2</sub>O.

**Author Contributions:** Conceptualization, J.Y.M., U.P., M.A., M.H. and S.; methodology, J.Y.M., U.P., M.A., M.H. and S.; software, M.A. and M.H.; validation, J.Y.M., M.A. and M.H.; formal analysis, J.Y.M., U.P. and S.; investigation, J.Y.M., U.P. and S.; data curation, J.Y.M. and U.P.; writing—original draft preparation, J.Y.M. and U.P.; writing—review and editing, J.Y.M., M.A. and M.H.; visualization, J.Y.M., S.W., H.H.B. and U.P.; supervision, J.Y.M., M.A. and M.H.; funding acquisition, U.P., S.W. and H.H.B. All authors have read and agreed to the published version of the manuscript.

**Funding:** This research was funded by the Academic Leadership Grant, grant number 2023/UN6.3.1/PT.00/2022. The research was also supported by the Tokyo Human Resources Scholarship fund.

**Institutional Review Board Statement:** Not applicable.

**Informed Consent Statement:** Not applicable.

**Acknowledgments:** We thank Universitas Padjadjaran for the Academic Leadership Grant and the Tokyo Metropolitan Government for the Tokyo Human Resources Scholarship fund. We also thank Professor Shinsuke Takagi of the Department of Applied Chemistry, Tokyo Metropolitan University, for the use of the electrochemical facilities.

**Conflicts of Interest:** The authors declare no conflict of interest.

## References

1. Yao, T.; An, X.; Han, H.; Chen, J.Q.; Li, C. Photoelectrocatalytic Materials for Solar Water Splitting. *Adv. Energy Mater.* **2018**, *8*, 1800210. [[CrossRef](#)]
2. Jiang, C.; Moniz, S.J.A.; Wang, A.; Zhang, T.; Tang, J. Photoelectrochemical devices for solar water splitting—Materials and challenges. *Chem. Soc. Rev.* **2017**, *46*, 4645–4660. [[CrossRef](#)] [[PubMed](#)]
3. He, Y.; Hamann, T.; Wang, D. Thin film photoelectrodes for solar water splitting. *Chem. Soc. Rev.* **2019**, *48*, 2182–2215. [[CrossRef](#)] [[PubMed](#)]
4. Walter, M.G.; Warren, E.L.; McKone, J.R.; Boettcher, S.W.; Mi, Q.; Santori, E.A.; Lewis, N.S. Solar Water Splitting Cells. *Chem. Rev.* **2010**, *110*, 6446–6473. [[CrossRef](#)]
5. Guo, L.; Chen, Y.; Su, J.; Liu, M.; Liu, Y. Obstacles of solar-powered photocatalytic water splitting for hydrogen production: A perspective from energy flow and mass flow. *Energy* **2019**, *172*, 1079–1086. [[CrossRef](#)]
6. Kanan, M.W.; Nocera, D.G. In Situ Formation of an Oxygen-Evolving Catalyst in Neutral Water Containing Phosphate and Co<sup>2+</sup>. *Science* **2008**, *321*, 1072–1075. [[CrossRef](#)]
7. Cheng, W.-H.; Richter, M.H.; May, M.M.; Ohlmann, J.; Lackner, D.; Dimroth, F.; Hannappel, T.; Atwater, H.A.; Lewerenz, H.-J. Monolithic Photoelectrochemical Device for Direct Water Splitting with 19% Efficiency. *ACS Energy Lett.* **2018**, *3*, 1795–1800. [[CrossRef](#)]
8. Ager, J.W.; Shaner, M.R.; Walczak, K.A.; Sharp, I.D.; Ardo, S. Experimental demonstrations of spontaneous, solar-driven photoelectrochemical water splitting. *Energy Environ. Sci.* **2015**, *8*, 2811–2824. [[CrossRef](#)]
9. May, M.M.; Lewerenz, H.-J.; Lackner, D.; Dimroth, F.; Hannappel, T. Efficient direct solar-to-hydrogen conversion by in situ interface transformation of a tandem structure. *Nat. Commun.* **2015**, *6*, 8286. [[CrossRef](#)]
10. Sun, K.; Liu, R.; Chen, Y.; Verlage, E.; Lewis, N.S.; Xiang, C. A Stabilized, Intrinsically Safe, 10% Efficient, Solar-Driven Water-Splitting Cell Incorporating Earth-Abundant Electrocatalysts with Steady-State pH Gradients and Product Separation Enabled by a Bipolar Membrane. *Adv. Energy Mater.* **2016**, *6*, 1600379. [[CrossRef](#)]
11. Safaei, J.; Ullah, H.; Mohamed, N.A.; Noh, M.F.M.; Soh, M.F.; Tahir, A.A.; Ludin, N.A.; Ibrahim, M.A.; Isahak, W.N.R.W.; Teridi, M.A.M. Enhanced photoelectrochemical performance of Z-scheme g-C<sub>3</sub>N<sub>4</sub>/BiVO<sub>4</sub> photocatalyst. *Appl. Catal. B Environ.* **2018**, *234*, 296–310. [[CrossRef](#)]
12. Mohamed, N.A.; Ullah, H.; Safaei, J.; Ismail, A.F.; Noh, M.F.M.; Soh, M.F.; Ibrahim, M.A.; Ludin, N.A.; Teridi, M.A.M. Efficient Photoelectrochemical Performance of  $\gamma$  Irradiated g-C<sub>3</sub>N<sub>4</sub> and Its g-C<sub>3</sub>N<sub>4</sub>@BiVO<sub>4</sub> Heterojunction for Solar Water Splitting. *J. Phys. Chem. C* **2019**, *123*, 9013–9026. [[CrossRef](#)]

13. Ullah, H.; Tahir, A.A.; Mallick, T.K. Structural and electronic properties of oxygen defective and Se-doped p-type BiVO<sub>4</sub>(001) thin film for the applications of photocatalysis. *Appl. Catal. B Environ.* **2018**, *224*, 895–903. [[CrossRef](#)]
14. Nasir, S.N.F.M.; Ullah, H.; Ebadi, M.; Tahir, A.A.; Sagu, J.S.; Teridi, M.A.M. New Insights into Se/BiVO<sub>4</sub> Heterostructure for Photoelectrochemical Water Splitting: A Combined Experimental and DFT Study. *J. Phys. Chem. C* **2017**, *121*, 6218–6228. [[CrossRef](#)]
15. Wang, S.; Liu, B.; Wang, X.; Zhang, Y.; Huang, W. Nanoporous MoO<sub>3-x</sub>/BiVO<sub>4</sub> photoanodes promoting charge separation for efficient photoelectrochemical water splitting. *Nano Res.* **2022**, *15*, 7026–7033. [[CrossRef](#)]
16. Tang, Y.; Jiang, D.; Wang, H.; Zheng, H.; Ren, L.; Wei, K.; Ma, W.; Dai, Y.; Luo, D.; Zhang, X.; et al. Band gap modulation of nanostructured WO<sub>3</sub> nanoplate film by Ti doping for enhanced photoelectrochemical performance. *J. Cent. South Univ.* **2022**, *29*, 2968–2979. [[CrossRef](#)]
17. Zhang, Y.; Huang, Y.; Zhu, S.; Liu, Y.; Zhang, X.; Wang, J.; Braun, A. Covalent S-O Bonding Enables Enhanced Photoelectrochemical Performance of Cu<sub>2</sub>S/Fe<sub>2</sub>O<sub>3</sub> Heterojunction for Water Splitting. *Small* **2021**, *17*, 2100320. [[CrossRef](#)]
18. Ullah, H.; Tahir, A.A.; Bibi, S.; Mallick, T.K.; Karazhanov, S.Z. Electronic properties of β-TaON and its surfaces for solar water splitting. *Appl. Catal. B Environ.* **2018**, *229*, 24–31. [[CrossRef](#)]
19. Yuan, S.-Y.; Jiang, L.-W.; Hu, J.-S.; Liu, H.; Wang, J.-J. Fully Dispersed IrO<sub>x</sub> Atomic Clusters Enable Record Photoelectrochemical Water Oxidation of Hematite in Acidic Media. *Nano Lett.* **2023**, *23*, 2354–2361. [[CrossRef](#)]
20. Wang, S.; He, T.; Yun, J.; Hu, Y.; Xiao, M.; Du, A.; Wang, L. New Iron-Cobalt Oxide Catalysts Promoting BiVO<sub>4</sub> Films for Photoelectrochemical Water Splitting. *Adv. Funct. Mater.* **2018**, *28*, 1802685. [[CrossRef](#)]
21. Humayun, M.; Ullah, H.; Cheng, Z.-E.; Tahir, A.A.; Luo, W.; Wang, C. Au surface plasmon resonance promoted charge transfer in Z-scheme system enables exceptional photocatalytic hydrogen evolution. *Appl. Catal. B Environ.* **2022**, *310*, 121322. [[CrossRef](#)]
22. Shen, S.; Lindley, S.A.; Chen, X.; Zhang, J.Z. Hematite heterostructures for photoelectrochemical water splitting: Rational materials design and charge carrier dynamics. *Energy Environ. Sci.* **2016**, *9*, 2744–2775. [[CrossRef](#)]
23. Sivula, K.; Zboril, R.; Le Formal, F.; Robert, R.; Weidenkaff, A.; Tucek, J.; Frydrych, J.; Grätzel, M. Photoelectrochemical Water Splitting with Mesoporous Hematite Prepared by a Solution-Based Colloidal Approach. *J. Am. Chem. Soc.* **2010**, *132*, 7436–7444. [[CrossRef](#)]
24. Abdi, F.F.; Han, L.; Smets, A.H.M.; Zeman, M.; Dam, B.; van de Krol, R. Efficient solar water splitting by enhanced charge separation in a bismuth vanadate-silicon tandem photoelectrode. *Nat. Commun.* **2013**, *4*, 2195. [[CrossRef](#)]
25. Jeon, T.H.; Choi, W.; Park, H. Cobalt–phosphate complexes catalyze the photoelectrochemical water oxidation of BiVO<sub>4</sub> electrodes. *Phys. Chem. Chem. Phys.* **2011**, *13*, 21392–21401. [[CrossRef](#)] [[PubMed](#)]
26. Liu, B.; Li, J.; Wu, H.-L.; Liu, W.-Q.; Jiang, X.; Li, Z.-J.; Chen, B.; Tung, C.-H.; Wu, L.-Z. Improved Photoelectrocatalytic Performance for Water Oxidation by Earth-Abundant Cobalt Molecular Porphyrin Complex-Integrated BiVO<sub>4</sub> Photoanode. *ACS Appl. Mater. Interfaces* **2016**, *28*, 18577–18583. [[CrossRef](#)] [[PubMed](#)]
27. Suryani, O.; Higashino, Y.; Mulyana, J.Y.; Kaneko, M.; Hoshi, T.; Shigaki, K.; Kubo, Y. A near-infrared organic photosensitizer for use in dye-sensitized photoelectrochemical water splitting. *Chem. Commun.* **2017**, *53*, 6784–6787. [[CrossRef](#)]
28. Lyon, L.A.; Hupp, J.T. Energetics of the Nanocrystalline Titanium Dioxide/Aqueous Solution Interface: Approximate Conduction Band Edge Variations between H<sub>0</sub> = −10 and H = +26. *J. Phys. Chem. B* **1999**, *103*, 4623–4628. [[CrossRef](#)]
29. Rothenberger, G.; Fitzmaurice, D.; Grätzel, M. Spectroscopy of conduction band electrons in transparent metal oxide semiconductor films: Optical determination of the flatband potential of colloidal titanium dioxide films. *J. Phys. Chem.* **1992**, *96*, 5983–5986. [[CrossRef](#)]
30. She, C.; Guo, J.; Lian, T. Comparison of Electron Injection Dynamics from Re-bipyridyl Complexes to TiO<sub>2</sub> Nanocrystalline Thin Films in Different Solvent Environments. *J. Phys. Chem. B* **2007**, *111*, 6903–6912. [[CrossRef](#)]
31. Zigler, D.F.; Morseth, Z.A.; Wang, L.; Ashford, D.L.; Brennaman, M.K.; Grumstrup, E.M.; Brigham, E.C.; Gish, M.K.; Dillon, R.J.; Alibabaei, L.; et al. Disentangling the Physical Processes Responsible for the Kinetic Complexity in Interfacial Electron Transfer of Excited Ru(II) Polypyridyl Dyes on TiO<sub>2</sub>. *J. Am. Chem. Soc.* **2016**, *138*, 4426–4438. [[CrossRef](#)] [[PubMed](#)]
32. Ding, X.; Zhang, L.; Wang, Y.; Liu, A.; Gao, Y. Design of photoanode-based dye-sensitized photoelectrochemical cells assembling with transition metal complexes for visible light-induced water splitting. *Coord. Chem. Rev.* **2018**, *357*, 130–143. [[CrossRef](#)]
33. Ashford, D.L.; Gish, M.K.; Vannucci, A.K.; Brennaman, M.K.; Templeton, J.L.; Papanikolas, J.M.; Meyer, T.J. Molecular Chromophore–Catalyst Assemblies for Solar Fuel Applications. *Chem. Rev.* **2015**, *115*, 13006–13049. [[CrossRef](#)] [[PubMed](#)]
34. Purnama, I.; Salmahaminati; Abe, M.; Hada, M.; Kubo, Y.; Mulyana, J.Y. Factors influencing the photoelectrochemical device performance sensitized by ruthenium polypyridyl dyes. *Dalton Trans.* **2019**, *48*, 688–695. [[CrossRef](#)]
35. Salmahaminati; Abe, M.; Purnama, I.; Mulyana, J.Y.; Hada, M. Density Functional Study of Metal-to-Ligand Charge Transfer and Hole-Hopping in Ruthenium(II) Complexes with Alkyl-Substituted Bipyridine Ligands. *ACS Omega* **2021**, *6*, 55–64. [[CrossRef](#)]
36. Pratomo, U.; Purnama, I.; Mulyana, J.Y. Photo-induced water oxidation via cascade charge transfer on nanostructured BiVO<sub>4</sub>/TiO<sub>2</sub> modified with dye and co-catalyst molecules. *Inorg. Chim. Acta* **2020**, *500*, 119223. [[CrossRef](#)]
37. Nazeeruddin, M.K.; Angelis, F.D.; Fantacci, S.; Selloni, A.; Viscardi, G.; Liska, P.; Ito, S.; Takeru, B.; Grätzel, M. Combined Experimental and DFT-TDDFT Computational Study of Photoelectrochemical Cell Ruthenium Sensitizers. *J. Am. Chem. Soc.* **2005**, *127*, 16835–16847. [[CrossRef](#)]
38. Hanson, K.; Brennaman, M.K.; Luo, H.; Glasson, C.R.K.; Concepcion, J.J.; Song, W.; Meyer, T.J. Photostability of Phosphonate-Derivatized, Ru<sup>II</sup> Polypyridyl Complexes on Metal Oxide Surfaces. *ACS Appl. Mater. Interfaces* **2012**, *4*, 1462–1469. [[CrossRef](#)]

39. Purnama, I.; Kubo, Y.; Mulyana, J.Y. A robust ruthenium complex with nonyl-substituted bpy ligand for dye-sensitized photoelectrochemical cell application. *Inorg. Chim. Acta.* **2018**, *471*, 467–474. [[CrossRef](#)]
40. Hoertz, P.G.; Chen, Z.; Kent, C.A.; Meyer, T.J. Application of High Surface Area Tin-Doped Indium Oxide Nanoparticle Films as Transparent Conducting Electrodes. *Inorg. Chem.* **2010**, *49*, 8179–8181. [[CrossRef](#)]
41. Farnum, B.H.; Morseth, Z.A.; Lapidus, A.M.; Rieth, A.J.; Hoertz, P.G.; Brennaman, M.K.; Papanikolas, J.M.; Meyer, T.J. Photoinduced Interfacial Electron Transfer within a Mesoporous Transparent Conducting Oxide Film. *J. Am. Chem. Soc.* **2014**, *136*, 2208–2211. [[CrossRef](#)] [[PubMed](#)]
42. Farnum, B.H.; Morseth, Z.A.; Brennaman, M.K.; Papanikolas, J.M.; Meyer, T.J. Driving force dependent, photoinduced electron transfer at degenerately doped, optically transparent semiconductor nanoparticle surface. *J. Am. Chem. Soc.* **2014**, *136*, 15869–15872. [[CrossRef](#)] [[PubMed](#)]
43. Farnum, B.H.; Nakada, A.; Ishitani, O.; Meyer, T.J. Bias-dependent oxidative or reductive quenching of a molecular excited-state assembly bound to a transparent conductive oxide. *J. Phys. Chem. C* **2015**, *119*, 25180–25187. [[CrossRef](#)]
44. Hamberg, I.; Granqvist, C.G.; Berggren, K.F.; Sernelius, B.E.; Engström, L. Band-gap widening in heavily Sn-doped In<sub>2</sub>O<sub>3</sub>. *Phys. Rev. B* **1984**, *30*, 3240–3249. [[CrossRef](#)]
45. Masaoki, F.; Toshiyuki, Y.; Shuichi, K.; Takashi, K.; Shunichi, N.; Mikiharu, K. Intramolecular Energy Transfer in Covalently Linked Polypyridine Ruthenium(II)/Osmium(II) Binuclear Complexes. Ru(II)(bpy)<sub>2</sub>Meppy–(CH<sub>2</sub>)<sub>n</sub>–MeppyOs(II)(bpy)<sub>2</sub> (n = 2, 3, 5, and 7). *Bull. Chem. Soc. Jpn.* **1991**, *64*, 1632–1640.
46. Mulyana, Y.; Weber, D.K.; Buck, D.P.; Motti, C.A.; Collins, J.G.; Keene, F.R. Oligonuclear polypyridylruthenium(ii) complexes incorporating flexible polar and non-polar bridges: Synthesis, DNA-binding and cytotoxicity. *Dalton Trans.* **2011**, *40*, 1510–1523. [[CrossRef](#)]
47. Mulyana, Y.; Collins, G.; Keene, R. Synthesis, nucleic acid binding and cytotoxicity of oligonuclear ruthenium complexes containing labile ligands. *J. Incl. Phenom. Macrocycl. Chem.* **2011**, *71*, 371–379. [[CrossRef](#)]
48. Frisch, M.J.; Trucks, G.W.; Schlegel, H.B.; Scuseria, G.E.; Robb, M.A.; Cheeseman, J.R.; Scalmani, G.; Barone, V.; Petersson, G.A.; Nakatsuji, H.; et al. *Gaussian 09*; Gaussian, Inc.: Wallingford, CT, USA, 2016.
49. Wasylenko, D.J.; Ganesamoorthy, C.; Koivisto, B.D.; Henderson, M.A.; Berlinguette, C.P. Insight into Water Oxidation by Mononuclear Polypyridyl Ru Catalysts. *Inorg. Chem.* **2010**, *49*, 2202–2209. [[CrossRef](#)]
50. Mulyana, Y.; Keene, F.R.; Spiccia, L. Cooperative effects in homogenous water oxidation catalysis by mononuclear ruthenium complexes. *Dalton Trans.* **2014**, *43*, 6819–6827. [[CrossRef](#)]
51. Concepcion, J.J.; Jurs, J.W.; Templeton, J.L.; Meyer, T.J. One Site is Enough. Catalytic Water Oxidation by [Ru(tpy)(bpm)(OH<sub>2</sub>)]<sup>2+</sup> and [Ru(tpy)(bpz)(OH<sub>2</sub>)]<sup>2+</sup>. *J. Am. Chem. Soc.* **2008**, *130*, 16462–16463. [[CrossRef](#)]
52. Berardi, S.; Francàs, L.; Neudeck, S.; Maji, S.; Benet-Buchholz, J.; Meyer, F.; Llobet, A. Efficient Light-Driven Water Oxidation Catalysis by Dinuclear Ruthenium Complexes. *ChemSuschem* **2015**, *8*, 3688–3696. [[CrossRef](#)] [[PubMed](#)]
53. Agnès, C.; Arnault, J.-C.; Omnès, F.; Jousset, B.; Billon, M.; Bidan, G.; Mailley, P. XPS study of ruthenium tris-bipyridine electrografted from diazonium salt derivative on microcrystalline boron doped diamond. *Phys. Chem. Chem. Phys.* **2009**, *11*, 11647–11654. [[CrossRef](#)] [[PubMed](#)]
54. Pan, Q.; Chen, T.; Ma, L.; Wang, G.; Hu, W.-B.; Zou, Z.; Wen, K.; Yang, H. Covalent Triazine-Based Polymers with Controllable Band Alignment Matched with BiVO<sub>4</sub> To Boost Photogeneration of Holes for Water Splitting. *Chem. Mater.* **2019**, *31*, 8062–8068. [[CrossRef](#)]
55. Takijiri, K.; Morita, K.; Nakazono, T.; Sakai, K.; Ozawa, H. Highly stable chemisorption of dyes with pyridyl anchors over TiO<sub>2</sub>: Application in dye-sensitized photoelectrochemical water reduction in aqueous media. *Chem. Commun.* **2017**, *53*, 3042–3045. [[CrossRef](#)] [[PubMed](#)]

**Disclaimer/Publisher's Note:** The statements, opinions and data contained in all publications are solely those of the individual author(s) and contributor(s) and not of MDPI and/or the editor(s). MDPI and/or the editor(s) disclaim responsibility for any injury to people or property resulting from any ideas, methods, instructions or products referred to in the content.